

Mesoscale variations of chemical and electronic landscape on the surface of Weyl semimetal $\text{Co}_3\text{Sn}_2\text{S}_2$ visualized by ARPES and XPS

Sudheer Anand Sreedhar,^{1,*} Matthew Staab,¹ Mingkun Chen,¹ Robert Prater,¹ Zihao Shen,^{1,†} Giuseppina Conti,² Ittai Sidilkover,^{3,4} Zhenghong Wu,^{5,‡} Eli Rotenberg,² Aaron Bostwick,² Chris Jozwiak,² Hadas Soifer,^{3,4} Slavomir Nemsak,^{2,1} Sergey Y. Savrasov,¹ Vsevolod Ivanov,^{6,7,8,§} Valentin Taoufik,¹ and Inna M. Vishik^{1,¶}

¹*Department of Physics and Astronomy, University of California, Davis, CA 95616, USA*

²*Advanced Light Source, Lawrence Berkeley National Lab, Berkeley, 94720, USA*

³*School of Physics and Astronomy, Faculty of Exact Sciences, Tel Aviv University, Tel Aviv-6997801, Israel*

⁴*Center for Light-Matter Interaction, Tel Aviv University, Tel-Aviv 6997801, Israel*

⁵*Department of Physics, Carnegie Mellon University, Pittsburgh, PA, 15213, USA*

⁶*Virginia Tech National Security Institute, Blacksburg, Virginia 24060, USA*

⁷*Department of Physics, Virginia Tech, Blacksburg, Virginia 24061, USA*

⁸*Virginia Tech Center for Quantum Information Science and Engineering, Blacksburg, Virginia 24061, USA*

(Dated: August 5, 2025)

The multiple crystalline terminations in magnetic Weyl semimetal $\text{Co}_3\text{Sn}_2\text{S}_2$ display distinct topological and trivial surface states, which have successfully been distinguished experimentally. However, a model of pure terminations is known to be inadequate because these surfaces exhibit a high degree of spatial heterogeneity and point disorder. Here we perform a spectromicroscopy study of the surface chemistry and surface electronic structure using photoemission measurements in combination with first-principles calculations of core levels. We identify an intermediate region with properties distinct from both the sulfur and tin terminations, and demonstrate that the spectral features in this region can be associated with a disordered tin termination with a varying density of surface tin-vacancies. Finally, we show how a combination of algorithmic and machine learning analysis of photoemission data can be used to extract identifying features, classify spatial regions, and correlate local chemistry with local electronic structure.

I. INTRODUCTION

Topological quantum materials feature bulk-boundary correspondence, whereby topological properties of the bulk are connected to gapless edge states [1]. Examples include linearly-dispersing surface bands with spin-momentum locking in topological insulators, hinge modes in higher-order topological insulators, and Fermi arcs in Weyl semimetals. What is sometimes less appreciated is that the chemical composition of the surface can strongly affect the presentation of characteristic surface states. This is because different surface terminations can have different polarity, dangling bonds, symmetries, disorder, or orbital content. This variability can lead to experimental ambiguities [2], but it can also be used as a tuning knob to drive the presentation of topological surface states within a single material [3–5].

In Weyl semimetals the characteristic Fermi arcs terminate at surface-projections of bulk Weyl points of opposite chirality [6]. The shape and length of Fermi arcs has implications for surface-dominated transport [7, 8], but bulk topology is only one factor in their morphology. Fermi arc length and connectivity can depend on surface termination, and can be tuned with surface dec-

oration and destroyed with strong disorder [4, 9–11]. An archetype of variable surface termination yielding different presentations of characteristic boundary states is $\text{Co}_3\text{Sn}_2\text{S}_2$, a magnetic Weyl semimetal on a kagome lattice [12–15]. Structurally, it can be viewed as repeating layers of $\text{Co}_3\text{Sn-S-Sn-S}$. The Co_3Sn termination has nanometer-scale lateral size and is primarily observed by nanoscale probes [16, 17]; it is predicted to yield short Fermi arcs connecting across Brillouin zones (BZs) [16]. The Sn and S terminations can have mesoscale extent, measuring up to tens of microns [18, 19]. The former has the cleanest presentation of long Fermi arcs connecting within the BZ, and most ARPES studies have focused here [12, 18]. The distance between the Sn and S layers in the crystal structure is smaller than their bond length, yielding irregular terminations and point defects which have been characterized by scanning tunneling spectroscopy [20, 21] but whose effect on mesoscale spectroscopic measurements has not been established. Here we show spatially-resolved ARPES and XPS data which identify and characterize the disordered region between pure terminations in $\text{Co}_3\text{Sn}_2\text{S}_2$. Additionally we discuss methods for visualizing and correlating these two streams of photoemission spectromicroscopy data.

II. METHODS

Single crystals of $\text{Co}_3\text{Sn}_2\text{S}_2$ were synthesized using solution growth. A ternary mixture with initial composition $\text{Co}_{12}\text{Sn}_{80}\text{S}_8$ was first heated to 400°C over two hours

* ssreedhar@ucdavis.edu

† zhshen17@gmail.com

‡ zhenghow@andrew.cmu.edu

§ vivanov@vt.edu

¶ ivishik@ucdavis.edu

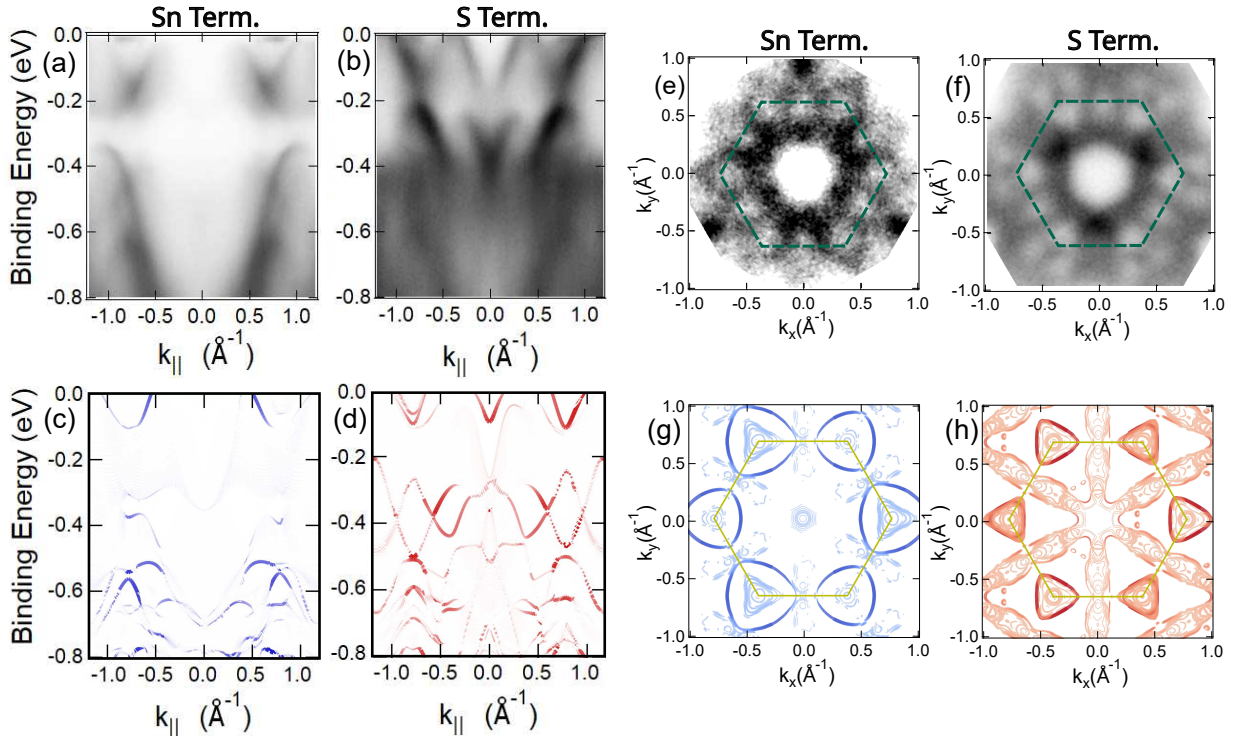


FIG. 1. Pure terminations of $\text{Co}_3\text{Sn}_2\text{S}_2$: ARPES. (a)-(b) ARPES spectra and (c)-(d) corresponding DFT slab calculation along the high-symmetry $\Gamma - K$ direction on the Sn (a,c) and S (b,d) termination, respectively. Only the surface bands are highlighted as colors in the calculations with blue representing Sn bands and red representing S bands (e)-(f) constant energy maps at E_F and (g)-(h) corresponding DFT-slab calculation on the Sn (e),(g) and S (f),(h) terminations, respectively. DFT colors heavily emphasize bands with strong surface character. Weyl points momenta are shown as green and pink dots in panel (e).

and held for another two hours. It was then heated to 1050°C over six hours and then held there for 10 hours, followed by slow cooling down to 740°C within 90 hours. The remaining flux was removed by centrifugation. Shiny hexagonal crystals were obtained. X-Ray powder diffraction data reports a hexagonal cell with $a = 5.3641 \text{ \AA}$ and $c = 13.1724 \text{ \AA}$ which are consistent with reported values [22].

Angle resolved photoemission spectroscopy (ARPES) and x-ray photoelectron spectroscopy (XPS) measurements were performed with microfocused synchrotron light at the Advanced Light Source MAESTRO beamline (7.0.2.1) and Beamline 5-2 at the Stanford Synchrotron Radiation Lightsource. All ARPES spectra shown here were obtained with photon energy 115 eV corresponding to $k_z = -0.086 \text{ \AA}^{-1}$, at normal emission, although nominal resolution does not allow this precise determination of k_z . This photon energy was previously determined to closely access the Weyl points which are located above the Fermi level (E_F) [12]. A nominal energy resolution of $\sim 20 \text{ meV}$ or better was used. $S-2p$ core levels were obtained with photon energy 250 eV and a nominal resolution better than $\sim 100 \text{ meV}$. Linearly polarized light was used in all measurements. Spectra were collected at a temperature $< 30\text{K}$, well below T_c . Samples were cleaved *in-situ* at the measurement temperature. Spatial

XPS and ARPES were obtained on a 25×15 grid with a spot size of $\sim 15 \mu\text{m}$.

First-principles calculations were performed using the Vienna ab initio Simulation Package (VASP) [23]. Standard hexagonal unit cells containing three $\text{Co}_3\text{Sn}_2\text{S}_2$ formula units were used to construct a $2 \times 2 \times 5$ unit cell slab containing 420 atoms for the surface state calculations. A vacuum of 50 \AA was introduced to electronically isolate the surfaces. Calculations were performed with no spin orbit coupling and an energy cutoff of 280 eV on a $3 \times 3 \times 1$ k -point grid. Core level energies were computed using the final state approximation; sulfur atoms near the center and surfaces of the cell were selected and an $S-2p$ core electron was removed and placed into the valence band. Additionally, sulfur core level calculations were performed with one or two of the tin atoms removed on the tin-terminated surface. Convergence of the binding energies was tested using unit cells ranging from $2 \times 2 \times 3$ (252 atoms) to $2 \times 2 \times 7$ (588 atoms) [24].

Core level simulations were performed using the Simulation of Electron Spectra for Surface Analysis package (SESSA)[25]. SESSA takes in crystal structure and chemistry information for a given geometry of a photoemission experiment to calculate the relative photoemission core level intensities observed using known electron attenuation lengths and photoemission cross-sections.

Due to the dependence of line widths on experimental conditions, we used line widths from the data in this manuscript as inputs for the simulated spectra. Where relevant, DFT was used to calculate chemical shifts in binding energies, which were then used as inputs for simulated spectra. More details of the crystal structure used can be found in the supplements [24].

III. RESULTS

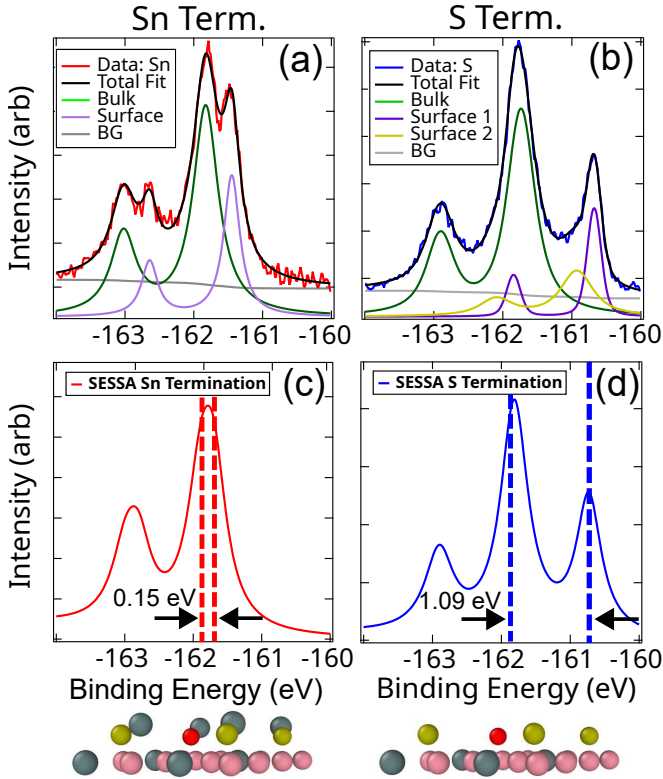


FIG. 2. $S-2p$ core levels on pure terminations. (a)-(b) $S-2p$ core levels on the Sn- and S- terminations. (c)-(d) SESSA simulation of the $S-2p$ XPS spectra at the two terminations using DFT-calculated binding energy shifts and attenuation based on the crystal structure [24]. Binding energy shifts indicated by vertical dashed lines and corresponding labels. Near-surface atomic planes with sulphur (yellow), tin (gray) and cobalt (pink) atoms. A photoemitting sulphur atom is marked red to disambiguate the emitter atom from the surface atom.

Fig. 1 reviews ARPES characteristics of the ‘pure’ Sn and S terminations, as previously established in refs [[16][18][26]]. The two terminations, measured at different positions on a single cleave, show distinct surface bands. Specifically, Fig. 1(b) shows strong features near Γ that are absent or minimal in Fig. 1(a). The surface-like nature of these features on the S termination is supported by DFT slab calculations, shown in Fig. 1(c)-(d). The calculations are colored to exclusively highlight the

surface bands; bulk features are discussed in earlier work [18], and do not differ between terminations. On the Sn termination, the dominant surface bands near E_F include those that form the Fermi arc surface state. Viewed as a function of momentum, the Fermi arcs of three adjacent BZs form ‘triangle-shaped’ features at three of the zone corners [12, 18, 19]. Meanwhile, the S termination shows weaker features at the zone corners, and stronger signatures of the dominant trivial surface state in the interior of the BZ. It is for these reasons that the Sn termination is the favored one for studying Weyl physics.

Core level photoemission intensity profiles are sensitive to local chemical environments, and the surface sensitivity of UV photoemission allows for detailed characterization of the surface chemistry [27, 28]. In $\text{Co}_3\text{Sn}_2\text{S}_2$, different surface terminations have been shown to manifest in core levels as follows. The Sn- $4d$ levels are shifted in energy slightly [19, 24]. The Co- $3p$ and Co- $3s$ levels tend to be broad and show minimal difference between

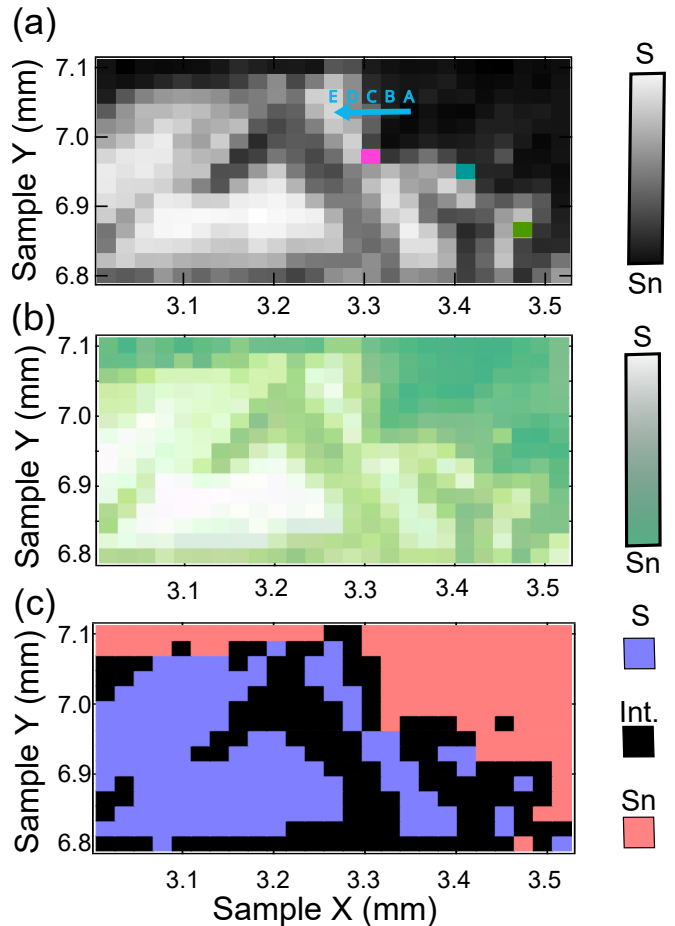


FIG. 3. Spatial dependence of $S-2p$ core levels. (a) Spatial map of $S-2p$ S-termination feature, found by integrating in energy window 160.8 ± 0.02 eV at each measurement position. (b) UMAP 3D performed on the same spatial core level data set (c) k-means clustering of the spatial core levels into 3 clusters representing S termination (blue), Tin Termination (Red) and Intermediate (Int.) region (black)

terminations [19, 24]. On the other hand the S-2*p* core levels show substantial variation in their structure depending on the local environment of the emitter, and are the focus of this work[26][29][18][30]. Fig. 2 summarizes the characteristics of the S-2*p* core level on the pure terminations. Fig. 2 (a)-(b) show spectra obtained at two different positions on the same crystal, together with fits. The Sn termination spectra can be fit by two Voigt doublets at different energies, while the S termination requires a third doublet. A Shirley Background, labeled ‘BG’, is used[31]. The spectra differ primarily via the energy position of the doublet at lower binding energy (purple curves in Fig. 2(a)-(b)) [18, 30, 32]. Based on photon-energy dependence experiments, this feature is interpreted to originate closer to the surface [24]. Meanwhile, the doublet at the deepest binding energy (green curves in Fig. 2(a)-(b)), is interpreted as originating from bulk sulphur atoms. Binding energy shifts between surface and bulk atoms are commonly observed in core level spectroscopy, and can arise due to both initial state and final state effects in the photoemission process [33][34]. To differentiate between these two possibilities, binding energy shifts between bulk and each pure surface termination are computed using DFT-based slab calculations. These calculations yield a surface core level shift of 0.19 eV (Sn termination) and 1.07 eV (S termination) relative to the bulk S-2*p* electron binding energies, in close agreement with experimental values of 0.33 eV and 1.09 eV respectively. The difference in binding energy between bulk and surface can, thus, largely be attributed to initial state effects from the unsatisfied valences at the surface. The deviations from experimental values may occur because of the finite cluster size of the calculations, core hole dynamics, and other final state effects that are neglected. Fig. 2 (c)-(d) shows SESSA simulated S-2*p* core level spectra, where core-level shifts of the S atoms closest to each surface are inputted from DFT.

Thus far, we have only shown spectra at single positions identified as pure terminations, but photoemission spectroscopies with small spot size can also be employed as spectromicroscopies to ascertain mesoscale electronic phenomena [35][36]. Fig. 3 examines the S-2*p* core level heterogeneity across a 0.5 mm × 0.3 mm area grid on the sample using three different visualization schemes. Fig. 3 (a) shows a spatial map that is produced by integrating the S-2*p* core level intensity at a binding energy of 160.8 ± 0.02 eV, to highlight the spatial variation of the spectral feature previously identified with surface component of the S-termination spectrum. The highest intensity regions on the map are interpreted as the S termination and the darkest regions as the Sn termination. Fig. 3(b) employs uniform manifold approximation and projection (UMAP) to project the high-dimensional photoemission spectra onto lower dimensional spaces, while preserving its topological structure [37]. Here, high-dimensional refers to the 800×1000 pixels in an ARPES spectrum or the 1000 pixels of an XPS data array. In Fig. 3(b), we apply UMAP to map every point on the spatial

grid of S-2*p* XPS spectra onto a 3D space. The resulting coordinates for each point are then mapped to a color scale. The generated color map closely resembles the intensity plot obtained in Fig. 3(a), but without use of user input. Because this method appears to capture the same spatial distributions as Fig. 3(a), we identify the dark green as ‘Sn termination’ and the white as ‘S termination’ on the color scale. As another way to characterize the different surface features, the spatial core level data were grouped into three clusters using k-means clustering [38–40] (Fig. 3(c)). These three clusters correspond closely to the regions in Fig. 3(a)-(b) identified as the S and Sn terminations, plus something in between. The latter is thereafter called the ‘intermediate region’.

XPS and ARPES provide two complementary information streams on the same cleave, so it is of interest to understand the correlation between the two: how much does a given local S-2*p* core level predict a local ARPES measurement and vice versa. Fig. 4 examines and correlates spatial ARPES and spatial XPS data collected on the same grid. This analysis is done for the entire data set and for each termination type individually. For the latter, groupings from Fig. 3(c) were used. To quantify the correlation between XPS and ARPES spectra, the following procedure is employed. First, all spectra were normalized to the background to account for differing photoemission intensity. For the core levels, this was done by dividing the spectra by the difference between intensity at the high and low binding energy tails outside the S-2*p* peak regions. For the ARPES spectra, integrated intensity above E_F was used to divide each spectra. Second, spectral differences for every pair of spatial points was calculated using the normalized spectra. An example of this difference for the core levels is shown in Fig. 4(a-c), wherein the difference (c) between spectra on two pure terminations S (a) and Sn (b) is demonstrated. The difference is also computed for the respective ARPES spectra in panels (d)-(f). Finally, each pairwise difference is reduced to a single number with a normalized absolute difference. These pairwise differences are summarized in Fig. 4(g)-(j), which show scatter plots of spectral differences for every pair of spatial points, where the x-axis is the difference in the XPS channel and the y-axis is the difference in the ARPES channel. The correlation within these scatter plots is then quantified using the Pearson correlation coefficient (Fig. 4(k)). A coefficient close to one indicates that data points exist on a tight diagonal where a small difference between two XPS spectra always implies a small difference between ARPES spectra and vice versa. The calculated Pearson coefficients for the full dataset, S, intermediate, and Sn termination are 0.95, 0.74, 0.74 and 0.81 respectively. This analysis suggests strong correlation between the local S-2*p* core levels and local ARPES spectra, especially when considering the entire data set. This result might not be surprising if only pure terminations are present, but in this data set, a large portion of the map consists of the intermediate region, whose disordered characteristics will be discussed

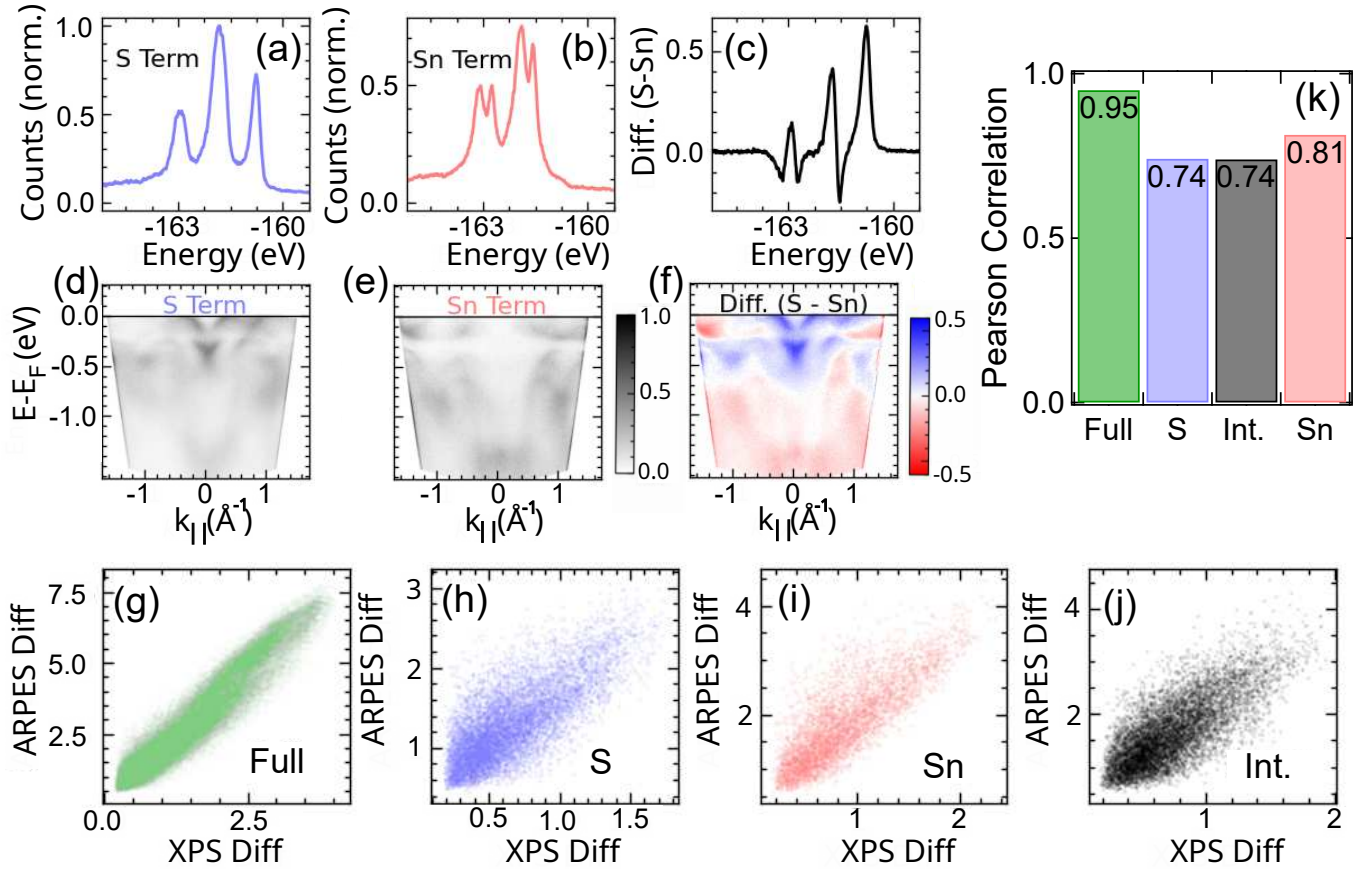


FIG. 4. Correlation between local S- $2p$ core levels and ARPES spectra. Example core levels for S (a) and Sn (b) termination as well as their difference, normalized to background (c). ARPES spectra for S (d) and Sn (e) termination and their difference (f). Scatter plots of XPS and ARPES difference metrics for the full data set (g), as well as S (h), Sn (i), and mixed (j) cluster subsets. (k) Pearson correlation between ARPES and S- $2p$ core level difference spectra for each of the previous clusters and the entire data set. Numbers are obtained values

next.

Guided by the correlation between spatially-resolved core level and ARPES data, Fig. 5 (a) and (b) further reduce the dimensionality of the UMAP color plots from Fig. 3(b), mapping the spatial ARPES and core level data onto a 2D space. The individual data points are color coded to match Fig. 3(b). This second step of dimensionality reduction is intended to highlight relationships between data points, but the x- and y-axes are not necessarily physically meaningful. The axis coordinates in UMAP are affected by the stochastic nature of the algorithm, thus, qualitative features are more reliable than absolute metrics in the resulting projection. This implies that while general relationships can be ascertained through UMAP, the relative distances of data can be misleading. Both 2D representations in Fig. 5(a)-(b) appear as a nearly one-dimensional meander, with points at either end corresponding to pure terminations and a gradual evolution in between. This indicates a continuous transition between the two terminations with contributions from multiple intermediate configurations between the two terminations. Two ways that a continuous evo-

lution of spectra can arise is 1) if all intermediate spectra are linear combinations of the two endpoints or 2) if spectral features evolve continuously between two endpoints but are not linear combinations of the two endpoints. Disambiguating between the two requires closer examination of the data.

Fig. 6 shows the typical evolution of the photoemission spectra for five adjacent positions traversing a termination change (blue arrow in Fig. 3(a)). The S- $2p$ core level is shown along the indicated trajectory in (a). Fits are performed for three selected spectra, labeled ‘A’, ‘C’ and ‘E’. A and E represent the pure Sn and S terminations, respectively, while C is representative of the ‘intermediate’ termination. Importantly, the fit for spectrum C includes an additional doublet with binding energy distinct from the surface-identified doublets observed for the two pure terminations. There is no way to produce spectrum C from a linear combination of the pure-termination spectra (A and E). This additional peak is also reminiscent of the third doublet (yellow) in Fig. 2(b), albeit with larger relative intensity. The broadness of the additional doublet suggests either the presence of multiple underly-

ing peaks and/or structural disorder. We contrast this with the evolution of ARPES spectra for the same five positions. The spectra shown in Fig. 6(b) reveal a gradual gain of spectral intensity near Γ when transitioning from the Sn to the S termination [24]. Meanwhile, at the M' point (vertical dashed lines in Fig. 6(b)), there is a gradual shift of spectral weight to deeper binding energies, which is quantified in the energy distribution curves (EDC) shown in Fig. 6(c). In the intermediate regions, signatures of both endpoint terminations coexist. Fig. 6(c) demonstrates this by fitting the traces of the intermediate region with linear combinations of spectra from the two terminations [24]. The percentage of S traces in the resulting fits are 6.3% (Red), 27.0% (Orange), 49.4% (Yellow), 69.0% (Green) and 87.9% (Blue) for the respective EDCs. The ARPES spectra in the intermediate region differ from the XPS spectra because it is possible to approximately treat the former as a linear combination of the pure endpoints. This distinction makes sense because dispersing valence bands arise from itinerant electrons and core levels are from localized electrons. We additionally note that ARPES spectra in the intermediate region (B-D) show enhanced spectral weight

at deeper binding energy at Γ [24], contributing to a ‘vertical dispersion’ feature, a motif that appears in systems with strong disorder [41].

To highlight the spectroscopic features of the intermediate region further, we select S-2*p* spectra from several other example spatial locations within the intermediate region, labeled with pink, dark blue, and green pixels in Fig. 3(a). These intermediate peaks can be mostly isolated by subtracting the dominant doublet associated with the bulk (green). An example of this is illustrated (pink) in Fig. 7(a) for data from the pink pixel in Fig. 3(a). Repeating this subtraction procedure at other positions, we find spectral intensity differences peaked at multiple binding energies across the intermediate region, highlighted by arrows at approximately ~ 162.6 eV, ~ 162.4 eV, ~ 162.1 eV and ~ 161.9 eV, as well as their spin-orbit-split pair, in Fig. 7(b). It is noted that the small peak at ~ 163.1 eV and its pair at ~ 161.8 eV are artifacts of incomplete bulk peak subtraction, and are thus not included in the labeling of various near-surface S-2*p* peaks. These multiple binding energies of near-surface S-2*p* states, Fig. 7 indicates multiple chemical environments of near-surface sulphur atoms. We capture the binding energy shifts of the near-surface S-2*p* core levels by considering different number of Sn vacancies above the sulphur layer using DFT. The calculations show increasing binding energy of the surface S-2*p* shoulder and the transformation of XPS line shape for an increasing number of Sn vacancies above a near-surface sulphur atom [24]. A photoemission experiment with a mesoscale spot size sees all of these spectral types superposed at each position. The simultaneous presence of these features along with the S termination shoulder in the experimental data presented in Fig. 6, in Fig. 2(b) and in 7(b) can be attributed to the macroscopic nature of our measurements compared to the nanoscale origin of these defects. To further model observed spectra in Fig. 7(b), the calculated binding energy shifts are used as inputs for SESSA simulations of XPS spectra for just the surface. Equal compositions of all the distinct surface states are used as an example. Qualitative agreement is shown; we note that the varying lineshapes of subtracted spectra in Fig. 7(b) suggests some mesoscale variation in concentration of each defect type.

IV. DISCUSSION

Prior work has demonstrated correspondence between DFT slab calculations and ARPES spectra on pure terminations [19][18][15]. Here, we extend these works by including DFT calculations of surface core level chemical shifts and considering the disordered intermediate region. When considering pure terminations (Fig. 2), the agreement between DFT and experiment suggests the following model for the surface core level binding energy shift. The S and Sn layers in the bulk crystal structure consist of alternating positive and negative oxidation states,

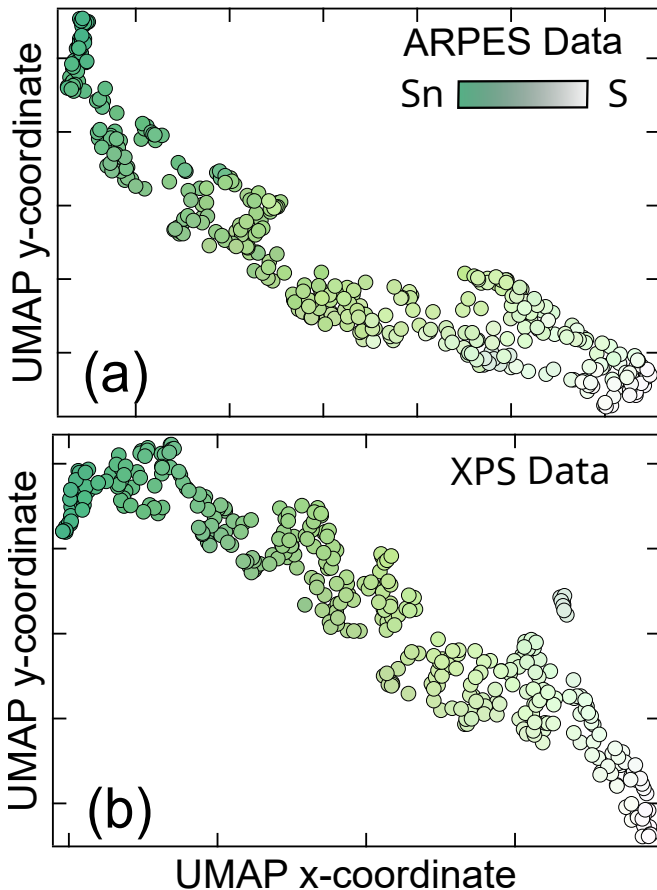


FIG. 5. UMAP on spatially resolved S-2*p* photoemission data. (a) 2D UMAP on spatial angle-resolved photoemission spectra. (b) 2D UMAP on spatial corelevel spectra.

with binding energies consistent with S^{2-} and Sn^{2+} [42]. Upon cleaving on a S termination, this surface consists of S atoms that would not have their valence satisfied. At the Sn surface, the $S-2p$ electrons are attracted to the Sn atoms above them, in contrast to the S termination. This produces a binding energy difference for the $S-2p$ electrons between the two terminations. Extending the aforementioned model to a Sn surface with missing atoms would imply that the S atoms surrounding these vacancies would have binding energy shifts intermediate between those of the pristine terminations. Fig. 7 confirms this hypothesis, demonstrating several discrete intermediate energy $S-2p$ binding energies with intensities

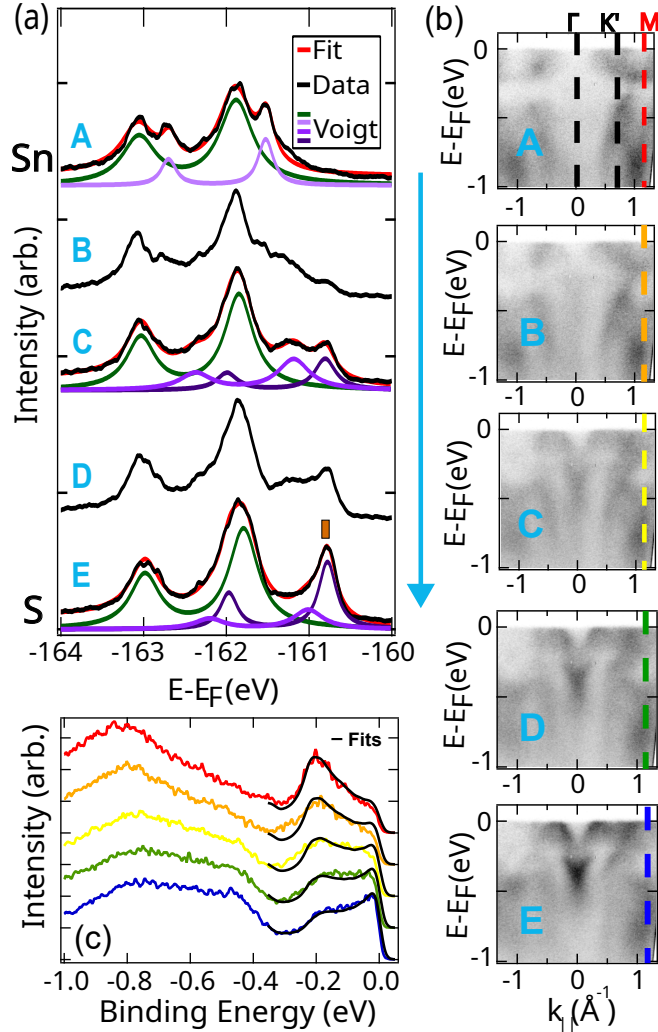


FIG. 6. Evolution of photoemission spectra between two pure terminations. (a) XPS spectra evolution from Sn to S termination; traces A-E correspond to spatial locations in line cut denoted by arrow in Fig. 3(a) and go from Sn termination (A) to Sn termination (E) across three intermediate spectra. (b) ARPES spectra along $\Gamma - K' - M'$ cut for the same spatial positions in a (c) EDCs at the M' point for each of the spectra in panel (b). Solid black lines are best fits of linear-combinations of spectra from Sn and S termination.

that vary between spatial points, presumably depending on vacancy concentrations. The presence of Sn vacancies has previously been reported on the UHV-cleaved surface of the material through large area STM studies[20], but their signature with the present mesoscale photoemission probe suggests that this constitutes a sizable fraction of the cleaved surface.

We now turn to more general implications of this study. First, we discuss the different spectromicroscopy data processing methods employed in this manuscript, and then turn to the broader ramifications of sequential measurements of local chemistry and local electronic structure.

Early work on identifying distinct surface terminations has relied on manual identification and correspondence with DFT. This is adequate for systems that have been studied before, systems that have very clear distinction between spectra on different terminations, and systems where DFT has good correspondence with ARPES spectra. $Co_3Sn_2S_2$ is an example of a system where a large portion of the cleaved surface shows spectra that are not pure terminations, and instead shows a continuum of ARPES spectra with different linear combinations of the two ‘pure’ terminations; materials like this can be ambiguous for manual identification based on ARPES spectra. Additionally, $Co_3Sn_2S_2$ shows only qualitative correspondence between ARPES spectra and DFT slab calculations: the preponderance of trivial surface states on the S termination and Fermi arcs that are sensitive to time-reversal symmetry breaking below T_c on the Sn termination are captured, but exact binding energies of features are not. It should be noted that the correspondence between experiment and DFT for the characteristic $S-2p$ core levels in this system is more exact.

Following manual identification of distinguishing spectral features, the spatial extent of each termination can be quantified by integrating over a chosen window in each photoemission spectrum in a spatial map. This has the advantage of being easy to implement, but the disadvantage of inadequacy with overlapping features and not being able to distinguish when there is low intensity due to the absence of a feature or due to a noisy spectrum.

The next level of spectral ‘grouping’ employed in this manuscript is k-means clustering, an unsupervised machine learning method to separate m data points into k clusters based on a sense of distance from the center of each cluster. This has the advantage of not relying on manual identification, but the disadvantage of requiring a user-chosen number of clusters. It is ideal for systems where there are a known/fixed number of spectral types, and less ideal when the number of ‘clusters’ is unknown or there is a continuum of spectra.

In this manuscript, we contrast these two methods with UMAP projected to three dimensions, which does not use experimenter-identified distinguishing spectral features or number of clusters. UMAP has emerged as a robust tool for dimensionality reduction because unlike algorithms such as principal component analysis (PCA)

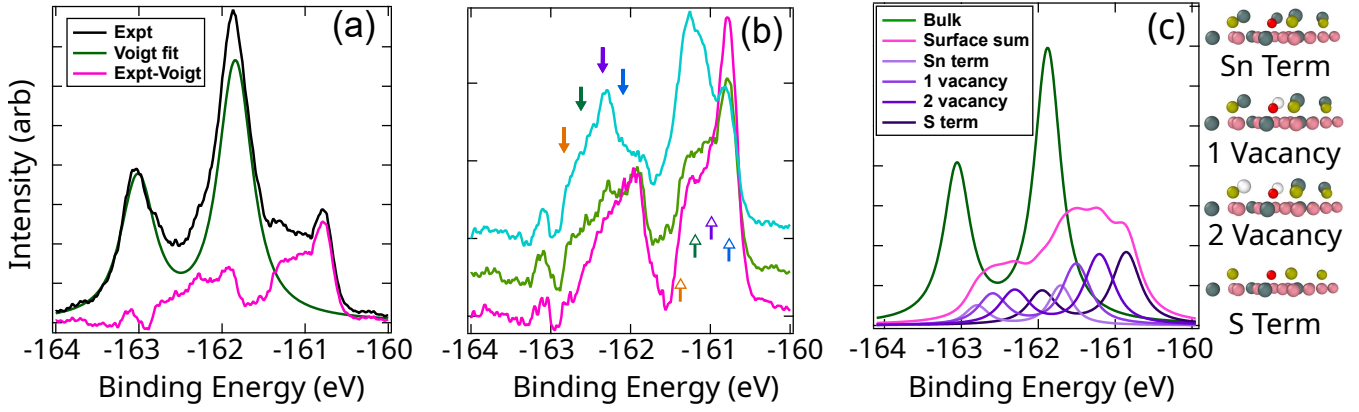


FIG. 7. Intermediate region S-2*p* surface spectra and simulations. (a) Spectrum at pixel marked in pink in Fig. 3(a), illustrating subtraction of bulk S-2*p* peak. (b) Example spectra following subtraction procedure in (a), with several distinct residual surface peaks highlighted by arrows. Colors correspond to spatial locations of the colored pixels in Fig. 3(a). (c) SESSA simulation of surface spectrum with an even coverage of four spectra indicated on right, using DFT-input binding energy shifts.

that perform linear dimensional reduction, UMAP leverages non-linear manifold learning to accurately capture both local neighborhoods and the broader global structure of the data [43]. Interestingly, a map produced in this manner is nearly indistinguishable from one produced by integrating the distinguishing portion of the spectra (Fig. 3(a)). As such, at least for $\text{Co}_3\text{Sn}_2\text{S}_2$, the more agnostic UMAP grouping appears to capture the salient features of the spatial distribution of different spectral types. Additionally, the UMAP analysis captures the smooth evolution between two endpoint spectra (pure terminations), which happens both in the ARPES and XPS channel, albeit with different manifestations.

S-2*p* spectra in this material have surface components with a set of discrete binding energies which cannot be reproduced from linear combinations of the endpoints. For the present data, the nonlinearity of UMAP dimensionality reduction is useful for capturing the subtle spectral variations within a macroscopic field of view. For assessing spectromicroscopy data for new materials, it can be instrumental for discovering how spatial data can be sorted into groups without prior knowledge of what the spectra look like.

Spatially-resolved ARPES spectra in $\text{Co}_3\text{Sn}_2\text{S}_2$ are generally a linear combination of the pure terminations, though deviations from this simple model in the intermediate region are intriguing demonstrations of spectral features that may arise from chemically disordered surface. This includes the appearance of a ‘vertical’ feature at normal emission discussed earlier, as well as the region near -0.3 eV binding energy (Fig. 6(c)) where intermediate-region spectra consistently exceed intensity of either pure termination. The fate of Fermi arcs in the intermediate region was not investigated here, but also merits further study, as the behavior of Fermi arcs amid surface disorder appears to depend on disorder strength [11, 44, 45]. Notably, $\text{Co}_3\text{Sn}_2\text{S}_2$ yields multiple disorder

environments within a single cleave, which can be identified from S-2*p* core levels using the methodology in this manuscript.

ARPES and XPS are measured with the same instrumentation which allows for sequential measurements of electronic structure and chemical composition within the same (near-surface) probing volume. Spatially-resolved techniques further allow for local lateral correspondence. Correlating these information streams is a generic problem with multiple manifestations: the present case of mixed cleave terminations, systems where chemical doping controls emergent behavior, and 2D materials with variable thicknesses on substrates.

In correlating local chemistry with local electronic structure, $\text{Co}_3\text{Sn}_2\text{S}_2$ presents a test case that has complications because of extended highly disordered regions that do not correspond to pure cleave terminations, but simplifications because the S-2*p* core level shows large changes in binding energy of its surface component, depending on local environment. The analysis in Fig. 4 presents one method for assessing how well local core level corresponds with a specific ARPES spectrum. When considering the entire field of view in the present data, the correlation is quite strong. Taken together with the UMAP, which showed a distinguishable ‘distance’ between pure Sn and pure S terminations in both XPS and ARPES, this indicates that in this system, one can identify the termination-type purely based on the S-2*p* core level. It should be noted that a single termination ‘type’ does not yield identical spectra, but there is also correlation between XPS and ARPES spectra *within* individual terminations, albeit weaker than when the entire field of view is considered. This finding is surprising for the intermediate region, which is defined by a high-degree of disorder.

For materials where local XPS spectra correspond reliably to specific ARPES spectra, there are implications

for experimental efficiency and accuracy. Core level spectra can often be collected faster, allowing this metric to be the more efficient choice for initial identification of spectral regions. A highly disordered surface can often yield diffuse and low-intensity valence bands, but can in certain cases, like the one illustrated here, be identified with XPS. Finally, cleaving can often bend the surface locally in different regions resulting in some mosaic spread in the crystal surface. Small tilt angles can have a very large effect on the bands but have hardly an effect on the core levels; in this scenario, core levels can identify different spatial regions as being similar whereas ARPES spectra alone might imply otherwise.

V. CONCLUSIONS

$\text{Co}_3\text{Sn}_2\text{S}_2$ has established itself as an important standard candle for implications of variable cleave terminations, because the characteristic Fermi arcs present distinctively on different surfaces. Prior ARPES literature has focused on identifying and measuring the *pure* terminations. In this paper, we delved into the less-discussed and highly disordered intermediate region, typically found between pure terminations, shedding light on how local defect environments produce characteristic S-2*p* surface states with discrete binding energies different from pure terminations. These characteristic local S-2*p* spectra correspond closely with specific ARPES spectra, making $\text{Co}_3\text{Sn}_2\text{S}_2$ a fruitful platform for investigating the effect of variable disorder on topological surface states. Additionally, we discussed different methods for finding structure

within multidimensional photoemission spectroscopy data, noting the propensity of UMAP to highlight small but relevant spectroscopic differences and identify relationships within data without user input.

ACKNOWLEDGMENTS

We acknowledge helpful discussions with Donghui Lu, Makoto Hashimoto, Journey Byland, Yucheng Guo, Maximilian Jaugstetter, Lorenz Falling, Jay Hineman, Alex Hexemer, Wiebke Köpp, and Tanny Chavez. The ARPES and XPS measurements in this work were supported by the US-Israel Binational Science Foundation Grant 2020067. Analysis of intermediate region data by MKC was supported by NSF-DMR 2428464. Use of the Stanford Synchrotron Radiation Lightsource, SLAC National Accelerator Laboratory, is supported by the U.S. Department of Energy, Office of Science, Office of Basic Energy Sciences under Contract No. DE-AC02-76SF00515. This research used resources of the Advanced Light Source, a U.S. DOE Office of Science User Facility under contract no. DE-AC02-05CH11231. SS and MS were supported in part by an ALS Doctoral Fellowship in Residence. VI acknowledges support from the National Science Foundation Growing Convergence Research Award 2428507. Z.S. and V.T. acknowledge the Cahill research fund for supporting sample synthesis

DATA AVAILABILITY

The data that support the findings of this manuscript will be made openly available following article acceptance.

-
- [1] A. M. Essin and V. Gurarie, *Phys. Rev. B* **84**, 125132 (2011).
 - [2] L. Li, K. Sun, C. Kurdak, and J. W. Allen, *Nature Reviews Physics* **2**, 463 (2020).
 - [3] H. F. Yang, L. X. Yang, Z. K. Liu, Y. Sun, C. Chen, H. Peng, M. Schmidt, D. Prabhakaran, B. A. Bernevig, C. Felser, B. H. Yan, and Y. L. Chen, *Nature Communications* **10**, 3478 (2019).
 - [4] A. S. Wadge, B. J. Kowalski, C. Autieri, P. Iwanowski, A. Hruban, N. Olszowska, M. Rosmus, J. Kołodziej, and A. Wiśniewski, *Phys. Rev. B* **105**, 235304 (2022).
 - [5] Z. Yue, J. Huang, R. Wang, J.-W. Li, H. Rong, Y. Guo, H. Wu, Y. Zhang, J. Kono, X. Zhou, Y. Hou, R. Wu, and M. Yi, *Nano Letters* **24**, 12413 (2024), doi: 10.1021/acs.nanolett.4c02846.
 - [6] B. Yan and C. Felser, *Annual Review of Condensed Matter Physics* **8**, 337 (2017).
 - [7] G. Resta, S.-T. Pi, X. Wan, and S. Y. Savrasov, *Phys. Rev. B* **97**, 085142 (2018).
 - [8] C. Zhang, Z. Ni, J. Zhang, X. Yuan, Y. Liu, Y. Zou, Z. Liao, Y. Du, A. Narayan, H. Zhang, T. Gu, X. Zhu, L. Pi, S. Sanvito, X. Han, J. Zou, Y. Shi, X. Wan, S. Y. Savrasov, and F. Xiu, *Nature Materials* **18**, 482 (2019).
 - [9] S. Souma, Z. Wang, H. Kotaka, T. Sato, K. Nakayama, Y. Tanaka, H. Kimizuka, T. Takahashi, K. Yamauchi, T. Oguchi, K. Segawa, and Y. Ando, *Phys. Rev. B* **93**, 161112 (2016).
 - [10] S. Hoffmann, S. Schimmel, R. Vocaturo, J. Puig, G. Shipunov, O. Janson, S. Aswartham, D. Baumann, B. Büchner, J. v. d. Brink, Y. Fasano, J. I. Facio, and C. Hess, *Advanced Physics Research* **4**, 2400150 (2025).
 - [11] C. Li, Y. Wang, J. Zhang, H. Liu, W. Chen, G. Liu, H. Deng, T. Kim, C. Polley, B. Thiagarajan, J. Yin, Y. Shi, T. Xiang, and O. Tjernberg, “Disorder driven non-anderson transition in a weyl semimetal,” (2024), arXiv:2402.14447 [cond-mat.mtrl-sci].
 - [12] D. F. Liu, A. J. Liang, E. K. Liu, Q. N. Xu, Y. W. Li, C. Chen, D. Pei, W. J. Shi, S. K. Mo, P. Dudin, T. Kim, C. Cacho, G. Li, Y. Sun, L. X. Yang, Z. K. Liu, S. S. P. Parkin, C. Felser, and Y. L. Chen, *Science* **365**, 1282 (2019), publisher: American Association for the Advancement of Science Section: Report.
 - [13] Q. Wang, Y. Xu, R. Lou, Z. Liu, M. Li, Y. Huang, D. Shen, H. Weng, S. Wang, and H. Lei, *Nature Com-*

- munications **9** (2018), 10.1038/s41467-018-06088-2.
- [14] H. Iohani, P. Foulquier, P. Le Fèvre, F. m. c. Bertran, D. Colson, A. Forget, and V. Brouet, *Phys. Rev. B* **107**, 245119 (2023).
- [15] H. Iohani, *Phys. Rev. B* **112**, 045140 (2025).
- [16] N. Morali, R. Batabyal, P. K. Nag, E. Liu, Q. Xu, Y. Sun, B. Yan, C. Felser, N. Avraham, and H. Beidenkopf, *Science* **365**, 1286 (2019).
- [17] S. Howard, L. Jiao, Z. Wang, N. Morali, R. Batabyal, P. Kumar-Nag, N. Avraham, H. Beidenkopf, P. Vir, E. Liu, C. Shekhar, C. Felser, T. Hughes, and V. Madhavan, *Nature Communications* **12**, 4269 (2021).
- [18] A. Rossi, V. Ivanov, S. Sreedhar, A. L. Gross, Z. Shen, E. Rotenberg, A. Bostwick, C. Jozwiak, V. Taufour, S. Y. Savrasov, and I. M. Vishik, *Phys. Rev. B* **104**, 155115 (2021).
- [19] F. Mazzola, S. Enzner, P. Eck, C. Bigi, M. Jugovac, I. Cocariu, V. Feyer, Z. Shu, G. M. Pierantozzi, A. De Vita, P. Carrara, J. Fujii, P. D. C. King, G. Vinai, P. Orgiani, C. Cacho, M. D. Watson, G. Rossi, I. Vobornik, T. Kong, D. Di Sante, G. Sangiovanni, and G. Panaccione, *Nano Letters* **23**, 8035 (2023), pMID: 37638737, <https://doi.org/10.1021/acs.nanolett.3c02022>.
- [20] J.-X. Yin, S. S. Zhang, G. Chang, Q. Wang, S. S. Tsirkin, Z. Guguchia, B. Lian, H. Zhou, K. Jiang, I. Belopolski, N. Shumiya, D. Multer, M. Litskevich, T. A. Cochran, H. Lin, Z. Wang, T. Neupert, S. Jia, H. Lei, and M. Z. Hasan, *Nature Physics* **15**, 443 (2019).
- [21] L. Jiao, Q. Xu, Y. Cheon, Y. Sun, C. Felser, E. Liu, and S. Wirth, *Physical Review B* **99**, 245158 (2019), publisher: American Physical Society.
- [22] Z. Shen, X. D. Zhu, R. R. Ullah, P. Klavins, and V. Taufour, *Journal of Physics: Condensed Matter* **35**, 045802 (2022).
- [23] G. Kresse and J. Furthmüller, *Phys. Rev. B* **54**, 11169 (1996).
- [24] The Supplemental Material at [URL will be inserted by publisher] contains further theoretical and experimental details.
- [25] W. Werner, W. Smekal, and C. J. Powell, “Simulation of electron spectra for surface analysis (sessa) version 2.2.2 user’s guide,” (2024).
- [26] D. F. Liu, A. J. Liang, E. K. Liu, Q. N. Xu, Y. W. Li, C. Chen, D. Pei, W. J. Shi, S. K. Mo, P. Dudin, T. Kim, C. Cacho, G. Li, Y. Sun, L. X. Yang, Z. K. Liu, S. S. P. Parkin, C. Felser, and Y. L. Chen, *Science* **365**, 1282 (2019).
- [27] D. Briggs and M. P. Seah, *Practical Surface Analysis by Auger and X-Ray Photoelectron Spectroscopy* (John Wiley, 1983).
- [28] D. Briggs, *Handbook of X-Ray and Ultraviolet Photoelectron Spectroscopy* (John Wiley, 1977).
- [29] Y. S. Dedkov, M. Holder, S. L. Molodtsov, and H. Rosner, *Journal of Physics: Conference Series* **100**, 072011 (2008).
- [30] L. Ma, N. A. I. Nemet, M. Bremholm, Z. Sun, A. K. Vestergaard, Z. Li, and J. V. Lauritsen, *Applied Surface Science*, 162046 (2024).
- [31] G. H. Major, N. Fairley, P. M. A. Sherwood, M. R. Linfoord, J. Terry, V. Fernandez, and K. Artyushkova, *Journal of Vacuum Science and Technology A* **38**, 061203 (2020).
- [32] G. Li, Q. Xu, W. Shi, C. Fu, L. Jiao, M. E. Kamminga, M. Yu, H. Tüysüz, N. Kumar, V. Süß, R. Saha, A. K. Srivastava, S. Wirth, G. Auffermann, J. Gooth, S. Parkin, Y. Sun, E. Liu, and C. Felser, *Science Advances* **5** (2019), 10.1126/sciadv.aaw9867.
- [33] W. Egelhoff, *Surface Science Reports* **6**, 253 (1987).
- [34] E. Rotenberg, J. D. Denlinger, U. Hessinger, M. Leskovaar, and M. A. Olmstead, *Journal of Vacuum Science and Technology B: Microelectronics and Nanometer Structures Processing, Measurement, and Phenomena* **11**, 1444 (1993).
- [35] H. Iwasawa, N. B. M. Schröter, T. Masui, S. Tajima, T. K. Kim, and M. Hoesch, *Phys. Rev. B* **98**, 081112 (2018).
- [36] H. Coy-Diaz, F. Bertran, C. Chen, J. Avila, J. Rault, P. Le Fèvre, M. C. Asensio, and M. Batzill, *physica status solidi (RRL) – Rapid Research Letters* **9**, 701 (2015).
- [37] L. McInnes, J. Healy, and J. Melville, “Umap: Uniform manifold approximation and projection for dimension reduction,” (2018), [arXiv:1802.03426 \[stat.ML\]](https://arxiv.org/abs/1802.03426).
- [38] H. Iwasawa, T. Ueno, T. Masui, and S. Tajima, *npj Quantum Materials* **7**, 24 (2022).
- [39] M. Imamura and K. Takahashi, *Scientific Reports* **14**, 24200 (2024).
- [40] P. Majchrzak, C. Sanders, Y. Zhang, A. Kuibarov, O. Suvorov, E. Springate, I. Kovalchuk, S. Aswartham, G. Shipunov, B. Büchner, A. Yaresko, S. Borisenko, and P. Hofmann, *Physical Review Research* **7** (2025), 10.1103/physrevresearch.7.013025.
- [41] S. T. Ciocys, Q. Marsal, P. Corbae, D. Varjas, E. Kennedy, M. Scott, F. Hellman, A. G. Grushin, and A. Lanzara, *Nature Communications* **15**, 8141 (2024).
- [42] E. Liu, Y. Sun, N. Kumar, L. Muechler, A. Sun, L. Jiao, S.-Y. Yang, D. Liu, A. Liang, Q. Xu, J. Kroder, V. Süß, H. Borrmann, C. Shekhar, Z. Wang, C. Xi, W. Wang, W. Schnelle, S. Wirth, Y. Chen, S. T. B. Goennenwein, and C. Felser, *Nature Physics* **14**, 1125 (2018).
- [43] J. Healy and L. McInnes, *Nature Reviews Methods Primers* **4**, 82 (2024).
- [44] P. Sessi, Y. Sun, T. Bathon, F. Glott, Z. Li, H. Chen, L. Guo, X. Chen, M. Schmidt, C. Felser, B. Yan, and M. Bode, *Phys. Rev. B* **95**, 035114 (2017).
- [45] R.-J. Slager, V. Juričić, and B. Roy, *Phys. Rev. B* **96**, 201401 (2017).

Supplementary Material: Mesoscale variations of chemical and electronic landscape on the surface of Weyl semimetal $\text{Co}_3\text{Sn}_2\text{S}_2$ visualized by ARPES and XPS

Sudheer Anand Sreedhar¹, Matthew Staab¹, Mingkun Chen¹, Robert Prater¹, Zihao Shen¹, Giuseppina Conti², Ittai Sidilkover^{3,4}, Zhenghong Wu⁵, Eli Rotenberg², Aaron Bostwick², Chris Jozwiak², Hadas Soifer^{3,4}, Slavomir Nemsak^{1,2}, Sergey Y. Savrasov¹, Vsevolod Ivanov^{6,7,8}, Valentin Taoufik¹, and Inna M. Vishik¹

¹Department of Physics and Astronomy, University of California, Davis, CA 95616, USA

²Advanced Light Source, Lawrence Berkeley National Lab, Berkeley, 94720, USA

³School of Physics and Astronomy, Faculty of Exact Sciences, Tel Aviv University, Tel Aviv-6997801, Israel

⁴Center for Light-Matter Interaction, Tel Aviv University, Tel-Aviv 6997801, Israel

⁵Department of Physics, Carnegie Mellon University, Pittsburgh, PA, 15213, USA

⁶Virginia Tech National Security Institute, Blacksburg, Virginia 24060, USA

⁷Department of Physics, Virginia Tech, Blacksburg, Virginia 24061, USA

⁸Virginia Tech Center for Quantum Information Science and Engineering, Blacksburg, Virginia 24061, USA

Supplementary Note 1: Convergence of core level calculations.

Slab Size	# of atoms	Binding energy, S-termination (eV)	Binding energy, Sn-termination (eV)
$2 \times 2 \times 7$	588	68.54024655	67.6419138
$2 \times 2 \times 6$	504	68.53135813	67.63895787
$2 \times 2 \times 5$	420	68.54031705	67.65324571
$2 \times 2 \times 4$	336	68.54417584	67.63852258
$2 \times 2 \times 3$	252	68.5406361	67.65256036
$2 \times 3 \times 4$	504	68.53947566	67.63363181

Table 1: S- $2p$ core level binding energies for a sulfur atom at the S surface termination and Sn surface termination for different slab sizes. The vacuum in all cases is 50 Å.

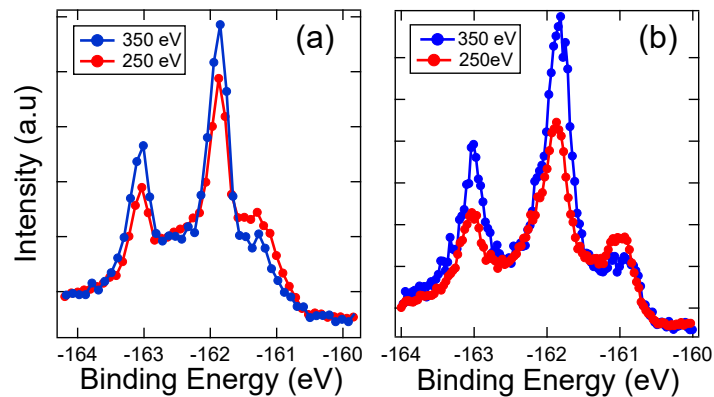


Figure S1: Photon Energy dependence of the S- $2p$ core level in (a) Sn Termination (b) S Termination. Core levels have been normalized for photon flux and photoionization cross-sections

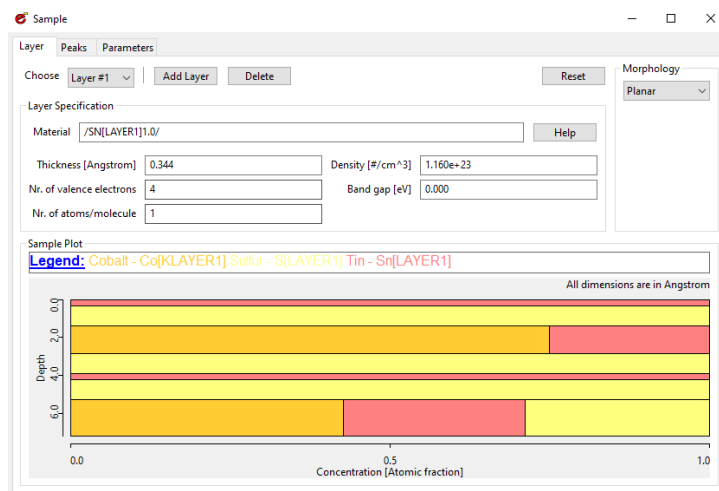


Figure S2: SESSA sample model. Atomic Densities were based on actual atomic densities of the layers in the crystal structure

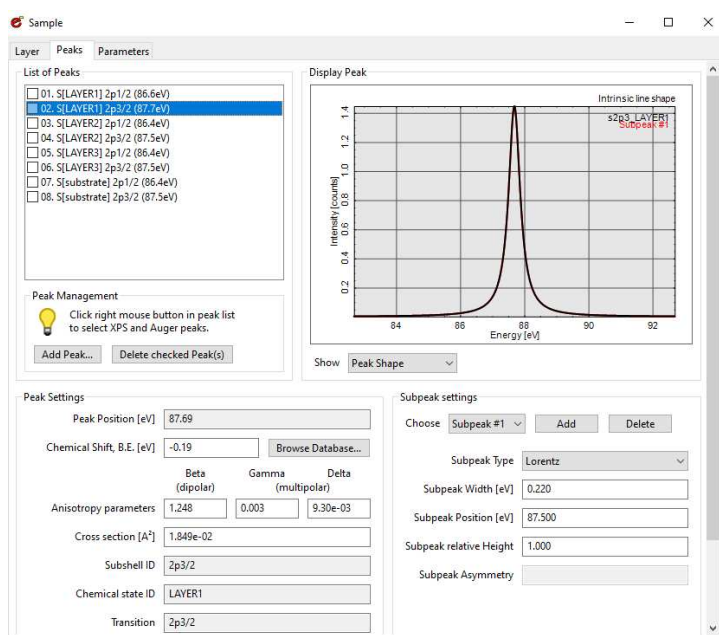


Figure S3: SESSA peaks panel containing details of peak offsets (from DFT) and line widths used

Supplementary Note 2: Determination of Bulk and surface features

Fig S1 shows Photon-flux and cross-section normalized S-2p core levels at 250 eV and 350 eV carried out on the same spot for both terminations. We observe intensity differences between the two photon energies for both terminations. Notably, intensity for the main peaks at ~ 163.1 eV and ~ 161.8 eV are both amplified while the shoulders at ~ 162.6 eV and ~ 161.3 eV in panel a (~ 162 eV and ~ 160.7 eV for panel b) are both mildly diminished with increasing photon energy. The calculated Inelastic Mean-free path using the TPP-2M[S1] formula at the two photon energies are 4.66 Å and 5.94 Å respectively. Based on the normalization, this difference can be attributed to the different depth sensitivity at both these photon energies.

Supplementary Note 3: Additional Details for SESSA simulation

Figures 2 and 7 in the main paper use SESSA to simulate XPS spectra. A layered model for the crystal was used for the simulation, as shown in Fig S2. Actual atomic densities for the material, from the crystal structure, were used. Atomic species were distinguished into surface and bulk, with only the surface atoms being given a chemical shift based on DFT calculations. Lorentzian line shapes with 0.22 eV widths were used for all peaks, as discussed in methods.

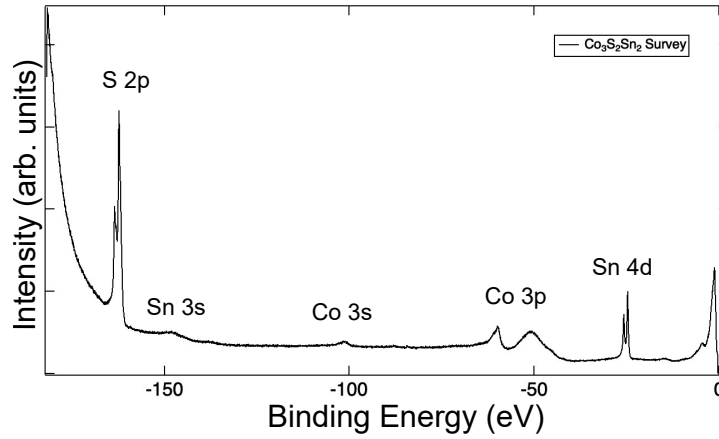


Figure S4: Survey of core levels in $\text{Co}_3\text{Sn}_2\text{S}_2$ at photon energy of 200 eV

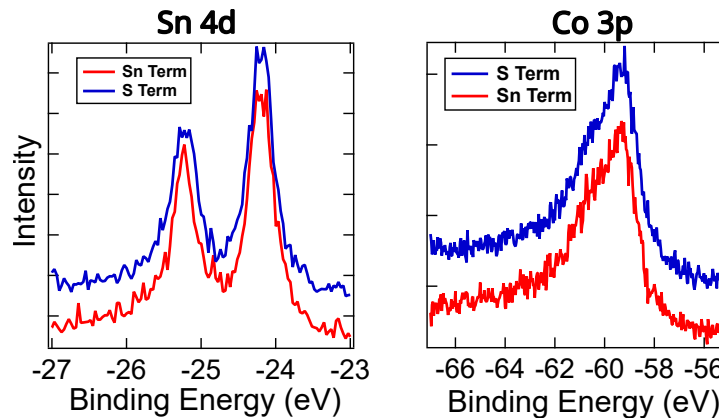


Figure S5: Sn-4d and Co-3p core levels taken at 250 eV

Supplementary Note 4

Fig. S4 and S5 show other relevant core levels that are not discussed in the main text where we focus on the information-rich S-2p core level. Fig. S4 shows a broad survey taken at 200 eV, which shows core levels corresponding to all elements in the compound. Further investigation at 250 eV of the Sn-4d and Co-3p levels (Fig. S5) indicates minimal differences at the two terminations as discussed in main text.

Supplementary Note 5

The main text references disorder-related effects on the presence of features exclusive to the intermediate region. We illustrate this in Fig. S6 with the EDCs at the Γ point for the same spatial points in Fig 6 of the main text. The raw EDCs of the intermediate region (Orange, Yellow and Green) very clearly demonstrate a pronounced increased intensity at approximately 0.85 eV binding energy. This highlighted feature manifests in the raw spectrum as a 'vertical' feature at normal emission, as discussed in main text. The prominent peak at around 0.4 eV binding energy in blue, green, and yellow EDCs is the distinct surface feature of the S termination, which is seen to become broader and weaker intensity in the intermediate region.

Supplementary Note 6

Fig 6 in the main text shows the results of a series of EDC fits to a few selected points in the spatial map at the M' point in the phase space. The fitting was conducted under the assumption that the EDC at each site consists of a linear combination of pure S-termination EDC and pure Sn-termination EDC. To further illustrate this idea, we demonstrate the result of the same fitting on the entire spatial map in Fig. S7. The pure terminations we selected using the UMAP analysis

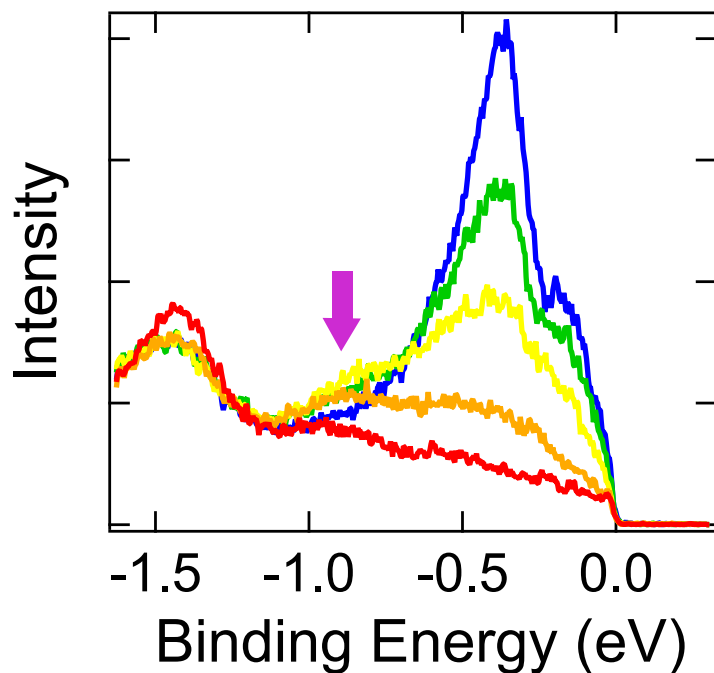


Figure S6: Raw EDC at Γ for spectra shown in Fig 6 of main text. Colors are consistent with main text figure. Arrow indicates additional spectral weight not found in ARPES spectrum of pure terminations

of Fig 3 from the main paper to find the 'purest' S and Sn terminations. Each EDC in the spatial data set is normalized to its area in the (-0.5,0) eV binding energy range and then fitted each to a linear sum as:

$$a \cdot \text{EDC}_S + (1 - a) \cdot \text{EDC}_{\text{Sn}} \quad (1)$$

Examples of these fits are shown in Fig. 6 of the main text.

The top (a-e) and middle panels (e-j) of Fig. S7 show the averaged ARPES and XPS spectra from points with different fitting parameters, which is essentially grouping different points in space by how much S content they have. In these averaged spectra, we can see the sulfur surface state feature at Γ diminishing as the fitting parameter goes to zero. These ARPES spectra are comparable to spectra from the intermediate region in Fig. 6b of the main text, though it should be noted that they are produced by averaging several spectra at different positions, rather than being individual spectra. Similarly, averaged S-2p core levels in Fig. S7 (f)-(j) show an evolving surface feature at low binding energy.

Supplementary Note 7

We also simulated core level spectra for the S-2p orbitals for different configurations of the surface vacancy (Fig. S8). DFT-calculated surface core level shifts were used for the SESSA simulation. We can clearly see the decreasing binding energy as we transition from the Sn termination to the S termination. It must be noted that pure vacancy terminations are hard to observe in photoemission spectra because of the macroscopic spot size. Thus, a superposition of each of these spectra is more likely observed.

References

- [S1] S. Tanuma, C. J. Powell, and D. R. Penn. Calculation of electron inelastic mean free paths (imfps) vii. reliability of the tpp-2m imfp predictive equation. *Surface and Interface Analysis*, 35(3):268–275, 2003. doi: <https://doi.org/10.1002/sia.1526>.

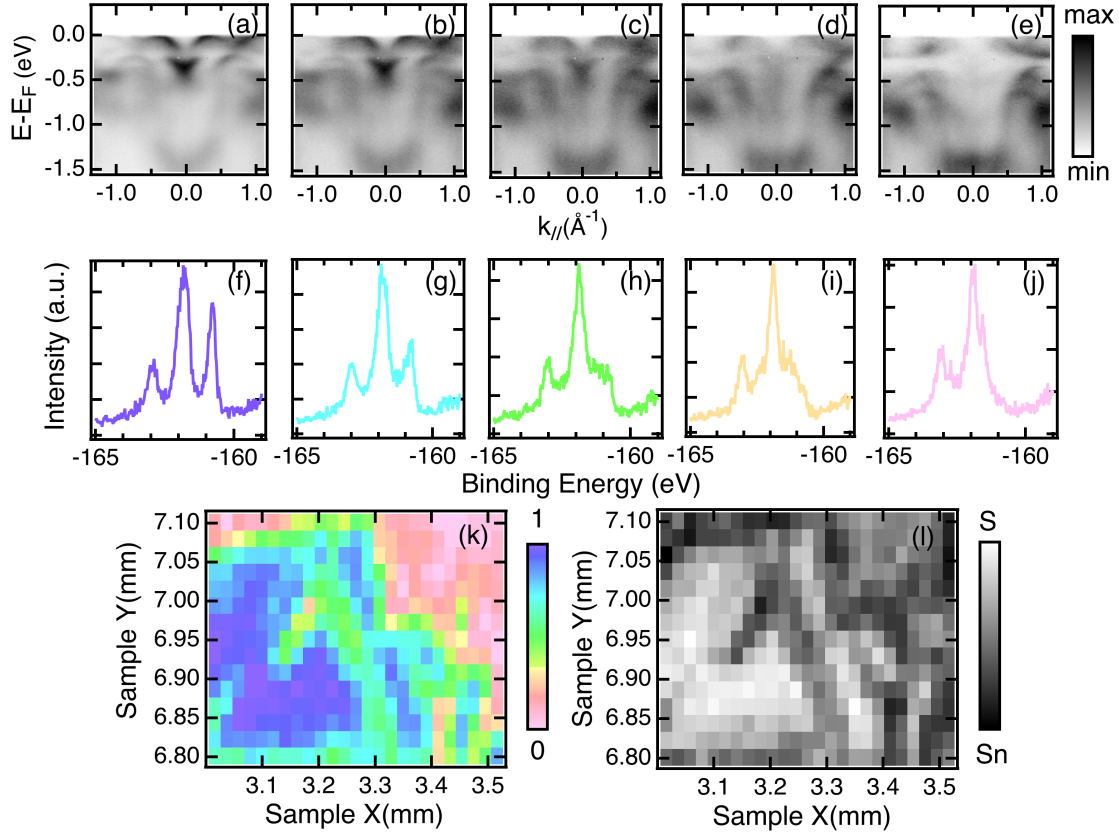


Figure S7: Global fitting of EDCs at M' point to linear combination of pure termination EDCs. Top panel (a)-(e), ARPES spectra from sites with fitting parameter (a in equation 1) 1, 0.75, 0.5, 0.25, 0 respectively. Each is an average of 5 spots with errors in the fitting parameter within ± 0.02 . Middle panel (f)-(j), Averaged $S-2p$ core level XPS spectra from the same spots as top panel. Color of each also corresponds to the map in the bottom panel. (k) Spatial variation of the fitting parameter. (l) Spatial map of $S-2p$ S-termination feature, same as in main text Fig 3(a).

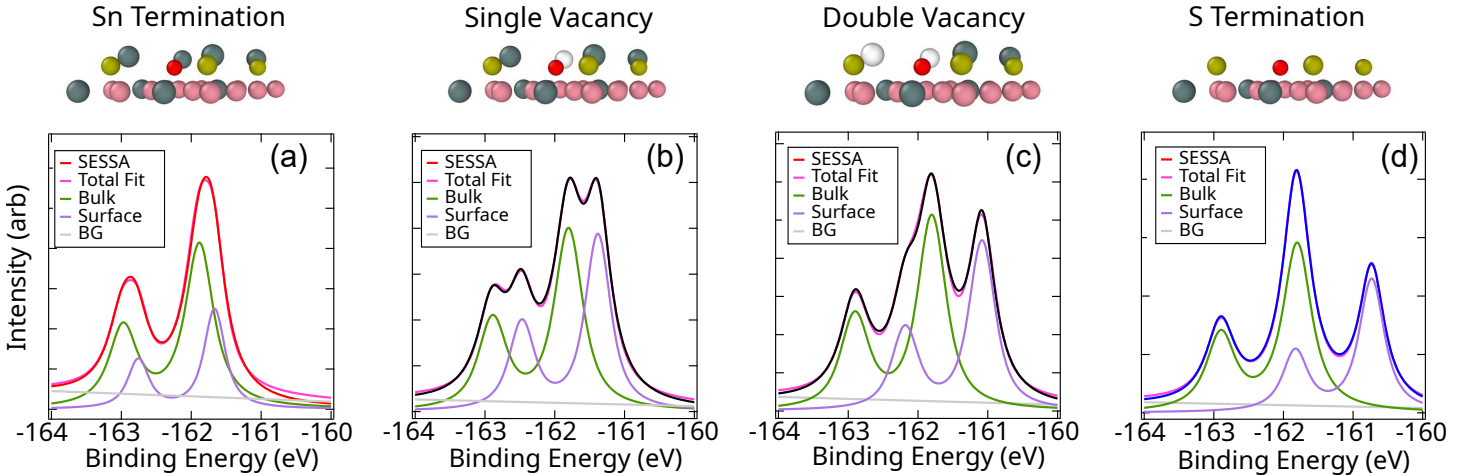


Figure S8: Simulations for different configurations of defects showing bulk $S-2p$ core level plus surface contribution from a single type of defect. a) Pure Sn termination b) Single vacancy c) Double vacancy d) Pure S termination. Chemical shift from DFT as discussed in methods.